ELSEVIER

Chemical Geology 225 (2006) 322–335

CHEMICAL GEOLOGY
INCLUDING
ISOTOPE GEOSCIENCE

www.elsevier.com/locate/chemgeo

Nanoscale phenomena during the growth of solid solutions on calcite {10$\bar{1}$4} surfaces

J.M. Astilleros [a,*], C.M. Pina [a], L. Fernández-Díaz [a], M. Prieto [b], A. Putnis [c]

[a] *Dpto. Cristalografía y Mineralogía, Universidad Complutense, 28040 Madrid, Spain*
[b] *Dpto. Geología, Universidad de Oviedo, 33005 Oviedo, Spain*
[c] *Institut für Mineralogie, Universität Münster, Corrensstraße 24, D-48149 Münster, Germany*

Accepted 16 August 2005

Abstract

This work deals with the growth behaviour of calcite {10$\bar{1}$4} surfaces in contact with multicomponent aqueous solutions containing divalent cations (Ba^{2+}, Sr^{2+}, Mn^{2+}, Cd^{2+}, or Mg^{2+}). The result is the formation of solid solutions, with calcite or aragonite as one of the end-members. In situ atomic force microscopy has revealed a wide variety of surface phenomena occurring during the formation of these solid solutions. Among them are: (1) the thickening of growth steps and the subsequent dissolution of surfaces followed by the nucleation of secondary three-dimensional nuclei on calcite surfaces, (2) the transition between growth mechanisms, (3) the formation of an epitaxial layer that armours the substrate from further dissolution and (4) the inhibitory effect of the newly formed surface on the subsequent growth (template effect). The two last phenomena can considerably limit coprecipitation as an effective mechanism for divalent metal uptake. All the phenomena described are a consequence of the interplay between thermodynamics, supersaturation of the aqueous solution with respect to the possible solid solutions and the crystallographic control of the surfaces on the cation incorporation, and indicates that there are many differences between the crystal growth of solid solutions and phases with fixed composition.

Keywords: Calcite; Solid solution–aqueous solution; Atomic force microscopy; Crystal growth; Mineral surfaces

1. Introduction

The incorporation of dissolved metals into the structure of minerals is an important process that can control their mobility and fate on the Earth's crust. Carbonate minerals, particularly calcite and aragonite, are among the most effective minerals capturing metals in aqueous environments. The so-called sorption processes (which include adsorption, absorption and co-precipitation) affect both the composition of natural waters and modify the surface structure and composition of the host mineral phase (Davis et al., 1987; Zachara et al., 1991; Tesoriero and Pankow, 1996). Many recent experimental works have been devoted to (i) detecting sorption processes by monitoring changes in the solution composition (Prieto et al., 2003; Godelitsas et al., 2003) and (ii) studying the chemical composition and structure of the mineral surface by surface-sensitive techniques (Stipp et al., 1992, 2003; Piriou et al., 1997; Sturchio et al., 1997, 1998; Reeder et al., 1999, 2000; Kelly et al., 2003).

Besides its importance in geochemistry and environmental sciences, the interactions of divalent metals

* Corresponding author. Tel.: +34 913944868; fax: +34 913944872.
E-mail address: jmastill@geo.ucm.es (J.M. Astilleros).

0009-2541/$ - see front matter © 2005 Elsevier B.V. All rights reserved.
doi:10.1016/j.chemgeo.2005.08.025

with mineral surfaces pose a large number of fundamental questions related to different aspects of mineral crystallization, including the influence of such metals in the formation of polymorphs, their effect as modifiers of the crystal morphology and their effectiveness as inhibitors of both nucleation and growth.

Although much effort has been devoted to improve our understanding of the thermodynamics and kinetics of solid solution precipitation (Glynn and Reardon, 1990; Prieto et al., 1997; Rimstidt et al., 1998; Glynn, 2000), there are many aspects of the process that still remain unknown. The nanoscale mechanisms of the process are among these aspects. The study of such molecular scale phenomena is especially relevant to understand the formation of crystals with a range of compositions. Growth and dissolution mechanisms of "pure" minerals have been extensively studied by in situ atomic force microscopy (AFM) (Hillner et al., 1992; Bosbach et al., 1995; Liang et al., 1996; Jordan and Rammensee, 1998; Pina et al., 1998a,b, 2000a; Jordan et al., 2001; Bokern et al., 2002; Shiraki et al., 2000; De Giudici, 2002). Phenomena such as the development of particular growth steps and two-dimensional nuclei shapes, growth anisotropy, and other surface processes occurring in the crystallization of solid solutions, can also be studied using an AFM. By comparing the characteristics and deviations of the growing surfaces of solid solutions with those corresponding to surfaces of pure substances (end-members), it is possible to obtain information about the nanometric-scale phenomena which lead to the growth of crystals with compositional variability (Pina et al., 2000b; Astilleros et al., 2000, 2002, 2003a,b).

In this study we describe and review in a common framework some nanoscale surface processes observed in a number of binary solid solution–aqueous solution systems. Some of these phenomena exclusively occur when calcite grows from a solution containing divalent cations larger than Ca^{2+}, while other have only been observed when growth occurred from a solution containing cations smaller than Ca^{2+}.

The interaction of solutions containing cations larger than Ca^{2+}(Ba^{2+} and Sr^{2+}) with calcite results in two interrelated effects:

- *Thickening of growth steps* due to the selective incorporation of such cations in calcite steps containing larger sites and *dissolution–recrystallization phenomena* after the initial formation of metastable layers of rhombohedral solid solutions.

In a different way, when solutions contain cations smaller than Ca^{2+}(Mn^{2+}, Cd^{2+} and Mg^{2+}), the following phenomena has been observed:

- *Transitions between growth mechanisms*. For instance, in the $(Mn,Ca)CO_3$–H_2O system, the addition of small amounts of Mn causes the transition from simple step advancement to a two-dimensional nucleation growth mechanism.
- *Inhibition of the sorption process due to the formation of a layer which armours the substrate.* This effect has been observed during the epitaxial growth of $CdCO_3$ on calcite.

Finally, we will devote another section to the *template effect*, which results from changes in calcite lattice parameters as a consequence of the incorporation of foreign cations. The new substrates inhibit the development of successive layers, leading to the reproduction of the original microtopography.

The understanding of all growth phenomena mentioned above requires a detailed knowledge of thermodynamics of SS–AS systems which is basically determined by the ideality of the solid solutions, and the difference in the solubility product of the end-members. Furthermore, since crystal growth takes place at the solid–aqueous solution interface, a complete picture of crystal structure, surface nanotopography and reactivity of the solid phase that acts as a substrate is needed.

2. Materials and methods

Nanoscale experiments were carried out using calcite $\{10\bar{1}4\}$ surface as substrate. The divalent cations substituting Ca^{2+} were Mg^{2+}, Mn^{2+}, Cd^{2+}, Sr^{2+}, and Ba^{2+}. All experiments were carried out at 25 °C in a fluid cell of a Digital Instruments Multimode Atomic Force Microscope (AFM) working in contact mode. Ca^{2+}–M^{2+}–CO_3^{2-} aqueous solutions were prepared by mixing Na_2CO_3, MCl_2 or $M(NO_3)_2$ and $CaCl_2$ aqueous solutions (where M = Ba, Sr, Mn, Cd, or Mg). The pH of the solutions was 10.20 ± 0.05 (see Astilleros et al., 2002, 2003a for details).

Because of the importance of Cd^{2+} as a contaminant, the sorption of this cation was also studied by carrying out macroscopic experiments. The experiments were performed at 25 °C and ambient CO_2 partial pressure, using calcite and aragonite as substrates. Thus, 2 g of aragonite or calcite $\{10\bar{1}4\}$ cleavage fragments (diameter: $1 < \varnothing < 1.5$ mm) were added to 100 cm^3 of reacting solution (see Prieto et al. (2003) for more details).

3. General nanometric features of the calcite {10$\bar{1}$4} face

Since crystallization processes take place at the solid–aqueous interface, a comprehensive study of such processes requires the knowledge of the crystal structure and surface microtopography of the substrate.

The orientation of growth steps and the height of elementary growth layers on calcite {10$\bar{1}$4} face can be satisfactorily explained by the periodic bond chain (PBC) model of Hartman and Perdok (1955). Calcite {10$\bar{1}$4} faces contain three non-equivalent PBCs oriented along <$\bar{4}$41>, <2$\bar{2}$1>, and <010> (Heijnen, 1985) and are, therefore, F faces (Fig. 1). Although all the steps parallel to a given set of PBCs are structurally identical, Staudt et al. (1994) pointed out that in the case of <$\bar{4}$41> non-equivalence arises when the sense of spreading is considered. There are four steps that are parallel to the <$\bar{4}$41> PBC: [$\bar{4}$41]$_+$, [48$\bar{1}$]$_+$, [$\bar{4}$41]$_-$, and [48$\bar{1}$]$_-$. The subscripts indicate opposite sense of advancement, according to the notation used by Staudt et al. (1994). Steps with the same subscripts are symmetrically related by a *c*-glide but no symmetry operation relates steps with different subscripts. Thus, [$\bar{4}$41]$_+$ and [$\bar{4}$41]$_-$ (or [48$\bar{1}$]$_+$ and [48$\bar{1}$]$_-$) are parallel, but move in opposite directions and are structurally non-equivalent. Kink sites in steps parallel to [$\bar{4}$41]$_+$ and [48$\bar{1}$]$_+$ are geometrically less constrained and can be described as larger kink sites. On the contrary, [$\bar{4}$41]$_-$ and [48$\bar{1}$]$_-$ steps contain "smaller" or more constrained kink sites. The geometry of the kink sites and their distribution between the four steps correlate with the observed anisotropy of both step growth and dissolution velocities in calcite (Hillner et al., 1992) (see Fig. 2).

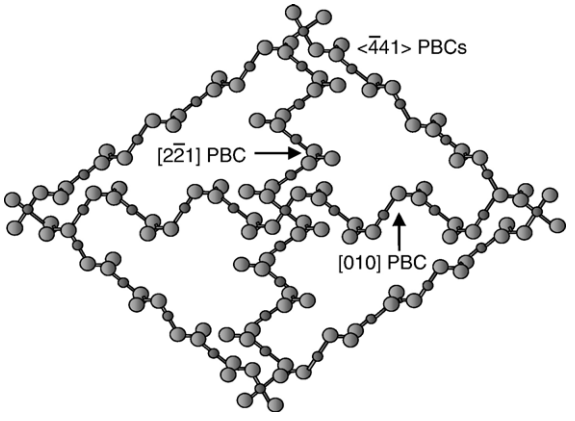

Fig. 1. Schematic illustration showing the three non-equivalent PBCs contained in the calcite {10$\bar{1}$4} face: two non-parallel <$\bar{4}$41> PBCs, which define the edge of the rhombohedron, and the PBCs <2$\bar{2}$1> and <010> parallel to the short and long diagonals. The straight PBCs parallel to <$\bar{4}$41> are the most stable, while the undulated PBCs parallel to <2$\bar{2}$1> and <010> have a higher energy and are less stable. The growth layers will be bounded by the most stable steps, i.e. those parallel to <$\bar{4}$41>. (After Paquette and Reeder, 1995).

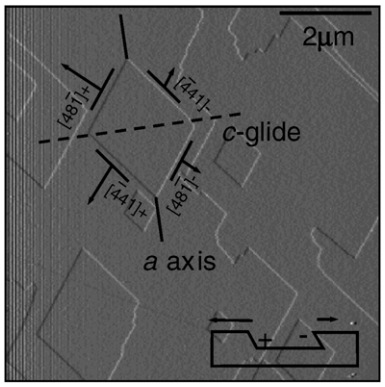

Fig. 2. AFM image of a calcite {10$\bar{1}$4} surface in water. On the dissolution pits, four non-equivalent steps parallel to <$\bar{4}$41>$_+$ and <$\bar{4}$41>$_-$, as well as the *a*-axis and the *c*-glide trace are indicated. Steps parallel to [$\bar{4}$41]$_-$ and [48$\bar{1}$]$_-$, i.e. those steps with constrained kink sites, exhibit a slow retreating speed, while those parallel to [$\bar{4}$41]$_+$ and [48$\bar{1}$]$_+$ retreat rapidly. The growth of this surface shows similar characteristics to dissolution, also occurring by a layer-by-layer mechanism with a clearly anisotropic advancement of monomolecular steps. Those steps parallel to [$\bar{4}$41]$_-$ and [48$\bar{1}$]$_-$ advance slowly while [$\bar{4}$41]$_+$ and [48$\bar{1}$]$_+$ advance rapidly. Such a coincidence reflects the crystallographic control of both processes.

Furthermore, the nonequivalence of growth steps has been considered by Staudt et al. (1994) and Paquette and Reeder (1990, 1995) and Reeder (1996) as the main reason for differential trace element incorporation in calcite structure (see Section 5).

4. Equilibrium and supersaturation in solid solution–aqueous solution (SS–AS) systems

Any study on crystal growth requires a previous knowledge of both the crystal–medium equilibrium conditions and the supersaturation. In solid solution–aqueous solution systems, the equilibrium relationships between solid and aqueous phase can be described by the formalism proposed by Lippmann (1980). The key concept in the Lippmann's model is the total solubility product, $\sum\Pi$, which can be expressed at thermodynamic equilibrium as a function of both the solid solution and the aqueous solution composition by means of the so-called *solidus* and *solutus* equations:

$$\Sigma\Pi_{eq} = K_{BA}a_{BA} + K_{CA}a_{CA} \qquad \text{solidus} \qquad (1)$$

$$\Sigma\Pi_{eq} = \frac{1}{\frac{X_{B,aq}}{K_{BA}\gamma_{BA}} + \frac{X_{C,aq}}{K_{CA}\gamma_{CA}}} \qquad \text{solutus} \qquad (2)$$

where $\Sigma\Pi_{eq}$ refers to the value of $\Sigma\Pi$ as specifically defined at thermodynamic equilibrium, K_{BA} and K_{CA} are the solubility products of the solid solution end-members, a_{BA} and a_{CA} are the activities of BA and CA in the solid, γ_{BA} and γ_{CA} are the solid phase activity coefficients and $X_{B,aq}$ and $X_{C,aq}$ are the activity fractions in the aqueous phase, of the B^+ and C^+ ions, respectively.

Curves described by Eqs. (1) and (2) can be plotted together to construct an equilibrium diagram in which $\Sigma\Pi_{eq}$ is represented on the ordinate and the composition of the solid and the aqueous solution in a double scale on the abscissa. Among the advantages of Lippmann's diagrams, it is worth mentioning that they allow us to easily visualize equilibrium compositional relationships between solid solutions and aqueous solutions, even for non-ideal solid solutions. In order to illustrate all these concepts, we have chosen the $(Sr,Ca)CO_3$–H_2O system as a model example.

Fig. 3a shows the Lippmann diagram corresponding to the $(Sr,Ca)CO_{3,orthorhombic}$–$H_2O$ system at 25 °C and 1 bar. The $(Sr,Ca)CO_{3,orthorhombic}$ is a subregular solid solution. Its non-ideality leads to the existence of an "eutectic" point on the solutus curve (left side of the diagram). The intersections of horizontal lines through the "eutectic" point with the solidus curve determine the miscibility gap of the solid solution. Out of the miscibility gap, coexisting solid and aqueous compositions at equilibrium are connected by tie lines.

Although at 25 °C and 1 atm the ionic radius of Sr^{2+} stabilizes $(Sr,Ca)CO_3$ solid solutions with an orthorhombic (aragonite-type) structure for a wide range of Sr substitution, $(Sr,Ca)CO_3$ solid solutions with a rhombohedral (calcite-type) structure can be also formed for low Sr content in the solid. Fig. 3b shows the Lippmann diagram for the $(Sr,Ca)CO_{3,rhombohedral}$–$H_2O$ system, considering that the $(Sr,Ca)CO_{3,rhombohedral}$ solid solution is a regular solid solution.

By superimposing the Lippmann diagrams for $(Sr,Ca)CO_{3,orthorhombic}$–$H_2O$ and $(Sr,Ca)CO_{3,rhombohedral}$–$H_2O$ systems, it is possible to construct a unified Lippmann diagram for the $(Sr,Ca)CO_3$–H_2O SS–AS system, where the stability fields for rhombohedral and orthorhombic phases can be defined (Fig. 4) (see Plumme and Busenberg, 1987; Böttcher, 1997; Astilleros et al., 2003a for a more detailed analysis of these solid solutions).

Lippmann diagrams can be constructed for any SS–AS system if the solubility of the end-members and the degree of ideality of the solid solution are known. However, in order to describe and interpret crystal growth experiments it is fundamental to evaluate the

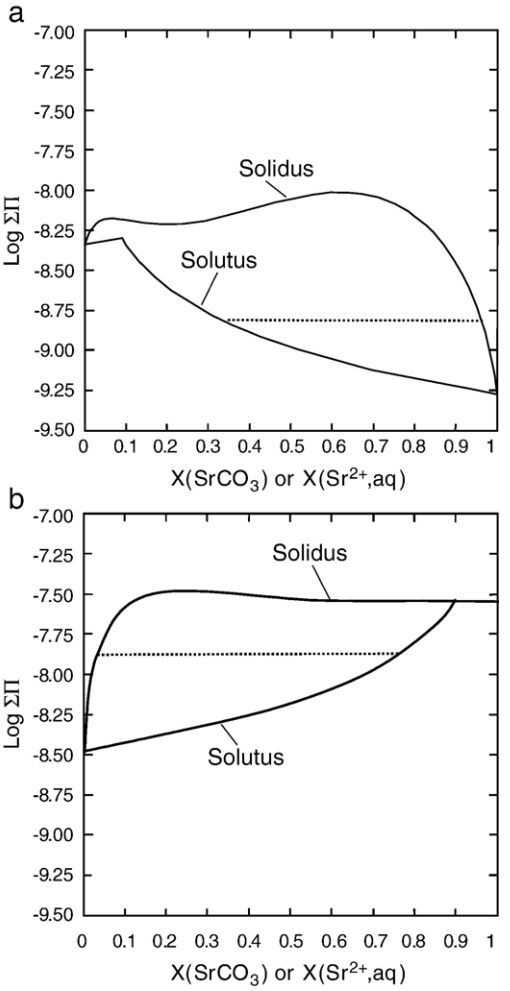

Fig. 3. Lippmann phase diagrams for the $(Ca,Sr)CO_3$ solid solution–aqueous solution systems at 25 °C: (a) $(Ca,Sr)CO_{3,orthorhombic}$–$H_2O$ system. The diagram was constructed assuming a subregular solid solution model with Redlich–Kister coefficients $a_0=3.43$ and $a_1=-1.82$; (b) $(Ca,Sr)CO_{3,rhombohedral}$–$H_2O$ system (Plummer and Busenberg, 1987). Diagram constructed considering a hypothetical regular solid solution model ($a_0=2.6$; Böttcher, 1997). In both diagrams, dotted tie lines connect solid–solution equilibrium pairs.

supersaturation of the aqueous solution with respect to the solid solution. The problem of evaluating supersaturations in SS–AS systems is not trivial and mathematical expressions have only been recently derived. At present there are two alternative formulations based, respectively, on the concept of stoichiometric saturation (see Glynn and Reardon, 1990) and on the two general equilibrium conditions for binary SS–AS systems:

$$[B^+]\,[A^-] = K_{BA}a_{BA} = K_{BA}X_{BA}\gamma_{BA} \tag{3a}$$

$$[C^+][A^-] = K_{CA}a_{CA} = K_{CA}X_{CA}\gamma_{CA} \tag{3b}$$

where X_{BA} and X_{CA} are the molar fractions of CA and BA in the solid solution and $[A^-]$, $[B^+]$ and $[C^+]$ are the activities of A^-, B^+ and C^+ ions in the aqueous solution.

The equation that describes the supersaturation by taking the stoichiometric saturation as a reference was given by Prieto et al. (1993):

$$\beta(X_{CA}) = \frac{[B^+]^{(1-X_{CA})}[C^+]^{X_{CA}}[A^-]}{(K_{BA}X_{BA}\gamma_{BA})^{(1-X_{CA})}(K_{CA}X_{CA}\gamma_{CA})^{(X_{CA})}} \quad (4)$$

As an alternative to $\beta(X_{CA})$ function, Astilleros et al. (2003c) have recently proposed the following supersaturation $\delta(X_{BA}, X_{CA})$ expression, directly derived from the thermodynamic conditions (3a) and (3b):

$$\delta(X_{BA}, X_{CA}) \begin{cases} \delta_{X_{BA}} = \frac{[A^-][B^+]}{X_{BA}\gamma_{BA}K_{BA}}, & \text{for} \quad X_{CA}^{eq} \geq X_{CA} \\ \delta_{X_{CA}} = \frac{[A^-][C^+]}{X_{CA}\gamma_{CA}K_{CA}}, & \text{for} \quad X_{CA}^{eq} \leq X_{CA} \end{cases} \quad (5)$$

where X_{CA}^{eq} is the molar fraction of the solid at equilibrium with respect to an aqueous solution of reference which has the same activity fraction as the given aqueous solution.

Fig. 5 shows the $\beta(X_{CA})$ and the $\delta(X_{BA}, X_{CA})$ supersaturation functions calculated for a given aqueous solution for the case of a hypothetical (B,C)A–H_2O system. It is worth noting that, although the derivations of $\beta(X_{CA})$ and the $\delta(X_{BA}, X_{CA})$ functions have two different starting points (i.e., the concept of stoichiometric saturation for $\beta(X_{CA})$ function and the two SS–AS equilibrium conditions for $\delta(X_{BA}, X_{CA})$ functions) both the maximum supersaturation and the supersaturation with respect to the end-members are coincident. This is a consequence of the concordance in the reference equilibrium states for these particular compositions. The choice of $\beta(X_{CA})$ or the $\delta(X_{BA}, X_{CA})$ functions to describe the saturation state in a SS–AS system will depend on the characteristics of the phenomena studied (congruent or incongruent dissolution, crystal growth of solid solutions with different degrees of ideality and kinetic restrictions, etc.). In this paper, we will use both supersaturation functions as reference parameters in the study of a number of crystal growth surface phenomena occurring during the crystallization of carbonate solid solutions.

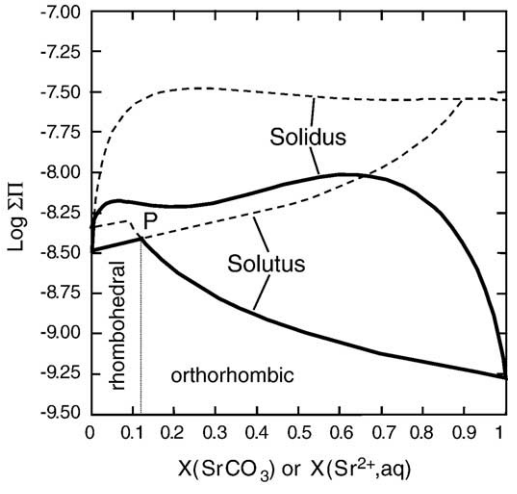

Fig. 4. Unified Lippmann phase diagram for the (Ca,Sr)CO_3 solid solution–aqueous solution system at 25 °C, constructed by combining Lippmann diagrams shown in Fig. 1 (Böttcher, 1997). Stability fields for the orthorhombic and rhombohedral phases are indicated (see Astilleros et al., 2003a for details).

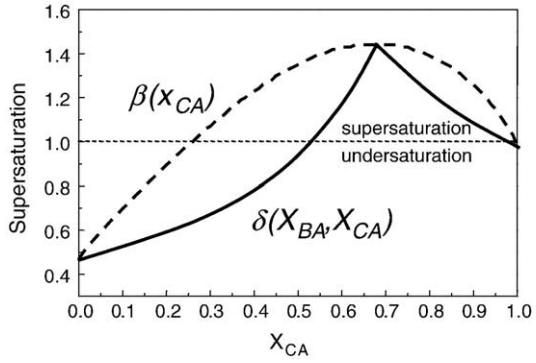

Fig. 5. Supersaturation functions, $\beta(X_{CA})$, and $\delta(X_{BA}, X_{CA})$ for a hypothetical and ideal $B_xC_{1-x}A$ solid solution (the solubility product of the end-members are: $K_{BA}=10^{-9.67}$ and $K_{CA}=10^{-9.99}$). These functions represent the supersaturation state of an aqueous solution with composition $[A^-]=[B^+]=[C^+]=1\times10^{-5}$ M with respect to the whole range of solid compositions. The dotted line represents saturation. The maximum supersaturation is reached for a solid with a molar fraction $X_{CA}=0.68$. Supersaturations given by both functions have the same value only for the end-members and a solid with $X_{CA}=0.68$.

5. Growth phenomena occurring in the presence of cations larger than Ca^{2+}: thickening of growth steps and dissolution recrystallization processes

In situ AFM observations of calcite $\{10\bar{1}4\}$ surfaces growing from solutions containing cations larger than Ca^{2+} (Ba^{2+} and Sr^{2+}) show that, when the concentration of the larger cation is high, an anomalous thickening of certain steps occurs. Fig. 6 shows an image of the calcite $\{10\bar{1}4\}$ surface growing from a Ba-rich solution where this microtopographic feature can be observed. In Fig. 6a, the step edges parallel to $[\bar{4}41]_+$, $[48\bar{1}]_+$, and $[010]_+$ contrast with the rest of the scanned area. These newly formed steps appear in a height image (Fig. 6b) as brighter areas than the original steps. This means that

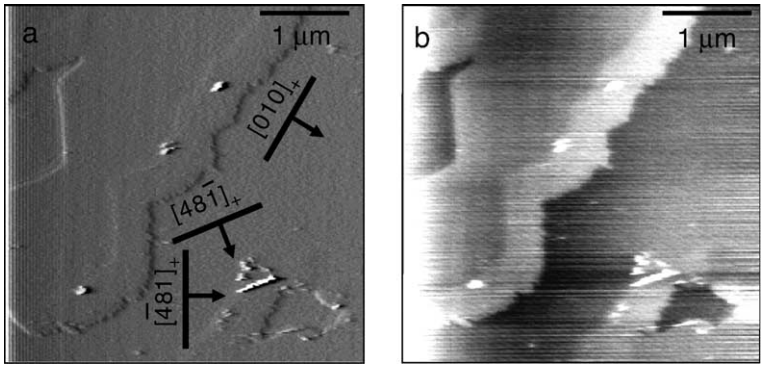

Fig. 6. Calcite {10$\bar{1}$4} surface in a supersaturated solution with respect to calcite ($\beta_{calcite}$=5); [Ba]=1.6 mmol/l. (a) AFM image took in constant force mode while displaying the cantilever deflection signal. The advance of jagged monomolecular [$\bar{4}$41]$_+$, [48$\bar{1}$]$_+$ and [010]$_+$ steps with a height of ~3 Å can be observed. The distance between lobes is around 40 nm. Note the different contrast of the newly grown step edges. (b) Height AFM image of the same area. The brighter step contours indicate that the newly grown steps are slightly thicker than the initial ones.

they correspond to higher areas in the calcite surface. Measurements indicate that, while the initial steps height was 3.0 Å, the newly grown steps are 4.6 Å thick. Similar microtopographic features can be observed on calcite {10$\bar{1}$4} surface growing from Sr-rich solutions. In this case, the thickness of the newly grown steps is 4.2 Å, i.e., they are 1.2 Å higher than the original ones (Astilleros et al., 2003b).

The anomalous thickening of the steps parallel to [$\bar{4}$41]$_+$ and [48$\bar{1}$]$_+$ is in agreement with the arguments of Paquette and Reeder (1990, 1995) and Staudt et al. (1994), who have shown that the nonequivalence of the two types of kinks along <$\bar{4}$41> controls the incorporation of trace elements into the calcite structure. According to their model, cations larger than Ca^{2+} (in the present case Ba^{2+} and Sr^{2+}) tend to incorporate in

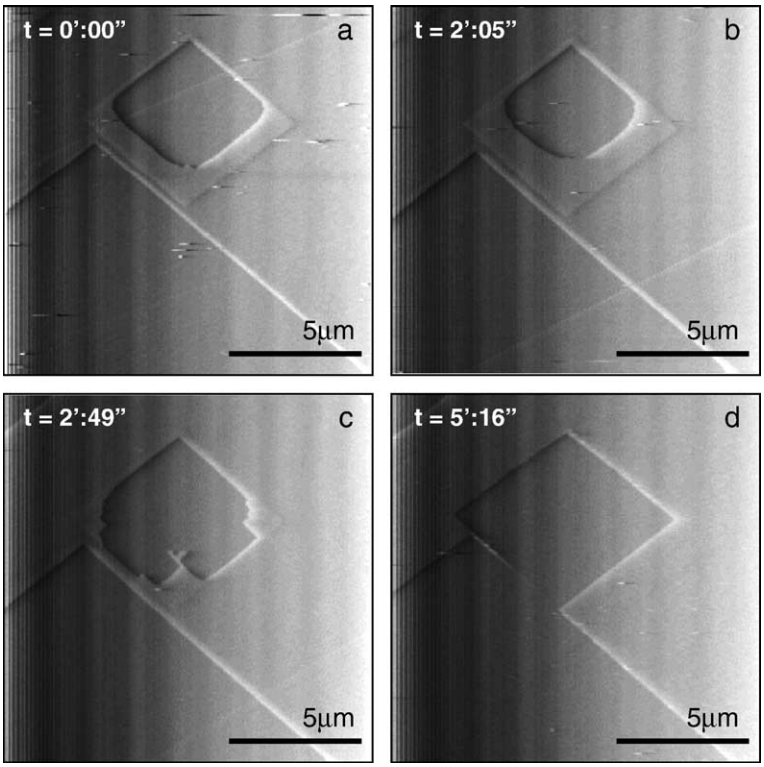

Fig. 7. AFM growth sequence on a calcite {10$\bar{1}$4} surface in contact with a solution supersaturated solution with respect to calcite ($\beta_{calcite}$=5); [Sr]=4.0 mmol/l (without flow). (a–b) The incorporation of Sr into the structure causes the thickening of advancing steps. (c–d) After some minutes, dissolution starts and the retreat of both the newly and the original steps can be observed. The time of the sequence is 316 s.

the steps with larger kink sites ($[\bar{4}41]_+$ and $[48\bar{1}]_+$), while cations smaller than Ca^{2+} (Mn^{2+}, Mg^{2+}, Cd^{2+}) will incorporate in the steps with constrained kink sites ($[\bar{4}41]_-$ and $[48\bar{1}]_-$). Because of the differences in ionic radii between Ca^{2+} (0.99 Å) and Ba^{2+} (1.34Å) and Sr^{2+} (1.18 Å), such preferential incorporation in $[\bar{4}41]_+$ and $[48\bar{1}]_+$ steps will cause an increase of the lattice parameters and, consequently, a thickening of these step edges.

This approach implicitly assumes that the incorporation of Ba^{2+} and Sr^{2+} into calcite occurs substituting for Ca^{2+}, i.e. by forming a solid solution. However, while the stable $CaCO_3$ structure at 25 °C and 1 atm is rhombohedral, $BaCO_3$ and $SrCO_3$ are orthorhombic. Thus, the equilibrium solubility of either Ba^{2+} or Sr^{2+} in the calcite structure is limited. The differences in thickness between "normal" calcite steps and newly-formed steps are too high to be explained by a low Ba or Sr content. On the other hand, the incorporation behaviour strongly depends on both aqueous solution composition and the supersaturation of the solutions with respect to the solid forming on the surface. In the experiments under consideration, the solutions were either Ba-rich or Sr-rich and the supersaturation levels with respect to $SrCO_3$ and $BaCO_3$ were relatively high ($\beta > 30$). Under such non-equilibrium conditions, a higher incorporation of the Ba or Sr than that thermodynamically stable may occur. Such a situation could explain to a certain extent the measured step thickness differences, although the incorporation of Ba and Sr also in nonlattice sites (Pingitore, 1986) cannot be excluded. The described behaviour implies a metastable situation that can be the starting point for subsequent dissolution–recrystallization reactions. In fact, along with the anomalous step thickening, a process of growth and subsequent coupled dissolution of surfaces and nucleation of secondary three-dimensional nuclei were observed. Such a process shows all the characteristics of a solvent-mediated transformation (Cardew and Davey, 1985; Davey and Garside, 2000). Fig. 7 shows how thick steps grow (a–b), partially closing an etch pit, then their advancement stops and, subsequently they begin to dissolve (c–d). The sequence corresponds to the interaction of an Sr-rich aqueous solutions with the calcite $\{10\bar{1}4\}$ surface. The removal of the thick steps occurs very rapidly. As soon as it finishes, dissolution of the original substrate starts, leading to a further opening of the etch pit. The subsequent inspection with AFM of different areas on the same calcite surface allows to observe that large three-dimensional nuclei

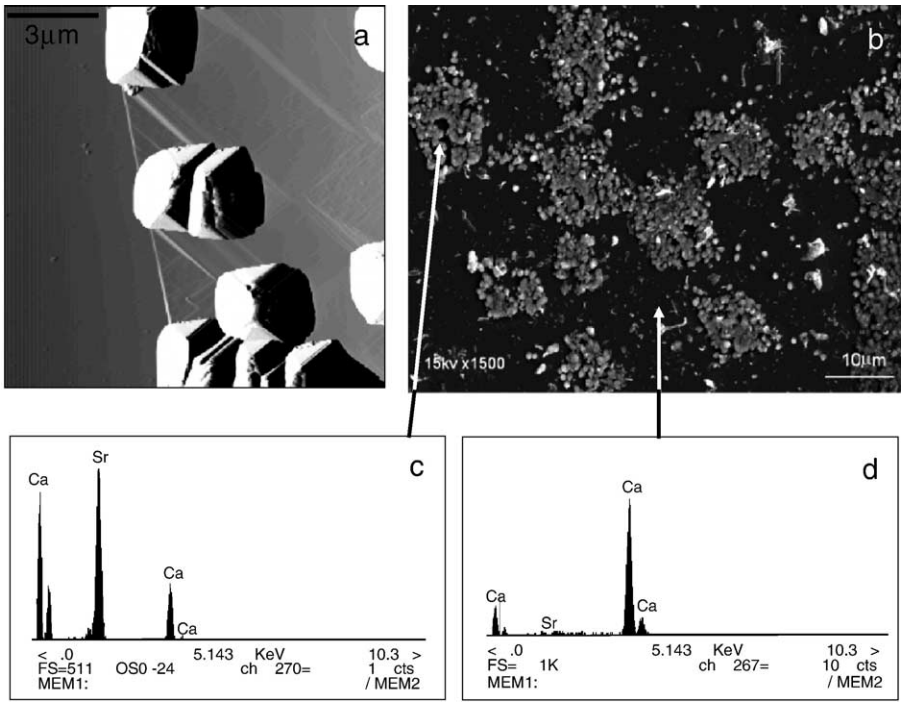

Fig. 8. (a) AFM image showing the formation of large three-dimensional nuclei of a new phase on calcite $\{10\bar{1}4\}$ surface (presumably Sr-rich orthorhombic phase). The nuclei are related to the dissolution of original steps showed in Fig. 7. The height of the nuclei is around 1 µm. (b) SEM image showing the distribution of the newly-formed crystals on $\{10\bar{1}4\}$ surface. The arrangement of the nuclei reproduces the shapes of etch pits. (c) EDX analysis of the newly-formed Sr-rich nuclei. (d) EDX analysis of the original calcite $\{10\bar{1}4\}$ surface.

of a new phase have formed simultaneously to the dissolution process (Fig. 8a). The subsequent ex situ observation of the surface by SEM indicates that there is a spatial relationship between the substrate dissolution and the formation of the three-dimensional nuclei, whose distribution reproduces the shape of etch pits (Fig. 8b). Moreover, the EDX analysis shows that the concentration of Sr in those nuclei is higher than in the rest of the areas (Fig. 8c–d).

As has been explained above, thick steps incorporate Sr and can be considered as a $(Sr,Ca)CO_{3,rhombohedral}$ solid solution, which can be metastable with respect to a certain $(Sr,Ca)CO_{3,orthorhombic}$ solid solution. In fact, the Sr-rich aqueous solution used in the experiments (Fig. 9) is supersaturated with respect to solid solutions with the calcite and aragonite structure. However, although for solids with a Ca-rich composition, the supersaturation values, with respect to calcite or aragonite type solid solutions, are similar, in the case of Sr-rich solid solutions, the supersaturation with respect to an aragonite-type phase is much higher than with respect to calcite-type solid solutions. Therefore, the formation of an orthorhombic Sr-rich solid solution should be favoured.

Initially, the calcite substrate allows the system to reduce its free energy by the formation of a metastable Sr-rich solid with a calcite structure. However, the high supersaturation with respect to the aragonite-type phase leads, after an induction period, to the formation of three-dimensional orthorhombic nuclei. Then, as a result of the growth of these nuclei, the solution becomes undersaturated with respect to the rhombohedral phase, which begins to dissolve. In turn, such dissolution results in an increase in the solution supersaturation with respect to the orthorhombic phase, which will continue growing. This produces a feedback effect that catalyses the dissolution of the metastable steps and the subsequent growth of the orthorhombic solid solution.

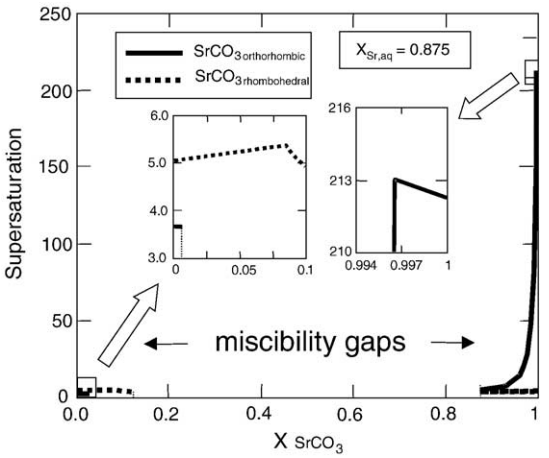

Fig. 9. Supersaturation functions, $\delta(X_{MnCO_3}, CaCO_3)$, for an aqueous solution of composition $[CaCl_2]=0.538$, $[Sr(NO_3)_2]=4.0$ and $[Na_2CO_3]=4.0$ mmol/l (see Fig. 8). The functions have not been drawn for the solid compositions in the miscibility gaps.

6. Growth phenomena occurring in the presence of cations smaller than Ca^{2+}

6.1. Transitions between growth mechanisms

In the layer-by-layer crystal growth regime the increase in supersaturation promotes a change in the growth mechanism from spiral growth to two-dimensional nucleation. For pure substances, the transitional supersaturation that separates these two basic growth mechanisms strongly depends on the solubility of the compound. Thus, under similar growing conditions (temperature, aqueous solution viscosity, etc.), sparingly soluble substances have higher transitional supersaturation values than compounds with high solubility (Sunagawa, 1987).

As we have seen previously, in the case of solid solutions the solubility varies from one end-member to the other (in different ways, depending on the degree of ideality of the solid solution). Therefore, for a given aqueous solution composition, a supersaturation distribution as a function of the solid solution composition is obtained. Under these circumstances, it is possible that supersaturations with respect to some solid solution compositions are high enough to overcome the energy barrier for two-dimensional nucleation, while other compositions can only grow according to the spiral growth mechanism. As a consequence, we can also expect a variation of the transitional supersaturations with the solid composition. There is experimental evidence (Pina et al., 2000b), also supported by recent theoretical developments (Pina et al., 2004), which indicates that the dependence of the transitional supersaturation on the solid composition is nearly linear.

Transition from the advancement of previous cleavage steps to the two-dimensional nucleation mechanism was observed in the experiments conducted in the $(Mn,Ca)CO_3$–H_2O SS–AS system. Fig. 10a shows the $\beta(X_{MnCO_3})$ supersaturation distributions calculated for three different aqueous solutions. As can be observed in Fig. 10b and c, when solutions 1 ($[MnCl_2]=0.01$ mmol/l) and 2 ($[MnCl_2]=0.025$ mmol/l) are used, growth on calcite $\{10\bar{1}4\}$ takes place exclusively by

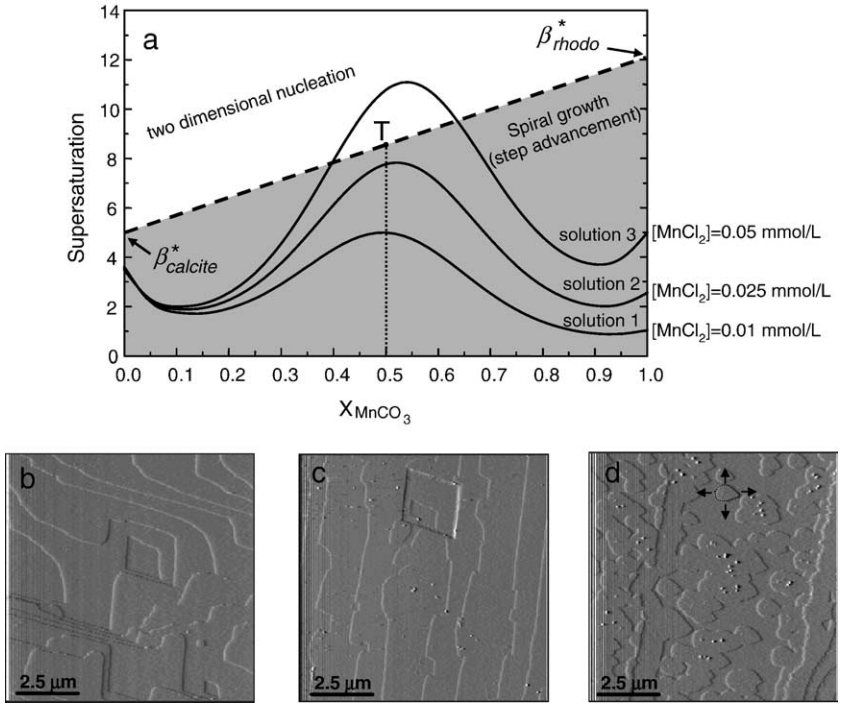

Fig. 10. (a) Supersaturation functions, $\beta(X_{MnCO_3})$, for the solutions 1, 2 and 3 calculated using Eq. (4) for the system (Ca,Mn)CO_3–H_2O. (b–d) Microtopography of the $\{10\bar{1}4\}$ surfaces growing from solutions 1, 2 and 3, observed by AFM. The observation of step advancement for solution 1 and 2 and two-dimensional nucleation only for solution 3 allows to draw the β^* line i.e., the variation of the transitional supersaturation between step advancement and two-dimensional nucleation as a function of the solid composition.

step advancement. This means that the generation of steps occurs exclusively on screw dislocations, spiral growth being the only mechanism that can perpetuate growth. In contrast, for solution 3 ([$MnCl_2$]=0.05 mmol/l) numerous two-dimensional nuclei rapidly appear randomly distributed on the surface (Fig. 10d). Transitional supersaturation for two-dimensional nucleation on pure calcite $\{10\bar{1}4\}$ surfaces is $\beta^*_{calcite} \approx 5$. Since transitional supersaturation values are strongly dependent on solubility, it is expected that β^* for pure $MnCO_3$ (rhodochrosite) will be higher than 5 ($K_{MnCO_3}=10^{-9.43}$; McBeath et al., 1998). Therefore, the transition from spiral growth to a two-dimensional nucleation mechanism presumably occurs for intermediate compositions of the $Mn_xCa_{1-x}CO_3$ solid solution ($X_{MnCO_3} \approx 0.5$) and between curves 2 and 3 (point T in Fig. 10a). By assuming a linear variation of the transitional supersaturation with the composition, the line connecting $\beta^*_{calcite}=5$ and the intermediate point T separates the regions corresponding to spiral growth and two-dimensional nucleation.

Diagrams similar to that shown in Fig. 10a can be constructed for any SS–AS system and for different surfaces. They provide a general view of the operating growth mechanisms as a function of the solid solution composition, constituting a useful tool to interpret growth behaviour in SS–AS systems.

6.2. Inhibition of the sorption process due to the formation of a solid solution thin layer

The fact that divalent metals (M^{2+}) can co-crystallize with calcium carbonate to form (M,Ca)CO_3 solid solutions implies that surface precipitation of solid solutions may be a significant mechanism of metal sorption onto calcite in aqueous environments. Ion partitioning during crystallization is controlled by both thermodynamics and kinetic/mechanistic factors (Lorens, 1981; Mucci and Morse, 1990; Paquette and Reeder, 1995). The difference in solubility of the solid solution end-members is one of these factors. In general terms, the lower the solubility of the metal-carbonate MCO_3 end-member the higher the tendency of this metal to incorporate into the solid phase, which is evident in the case of cadmium, where the extremely low solubility of otavite ($CdCO_3$) ($K_{sp,\ otavite}=10^{-12.1}$, Stipp et al., 1993) compared to that of pure calcite ($K_{sp,\ calcite}=10^{-8.48}$) (Plummer and Busenberg, 1982) results in a strong preferential partitioning of cadmium into the solid phase. Therefore, calcite should be a good

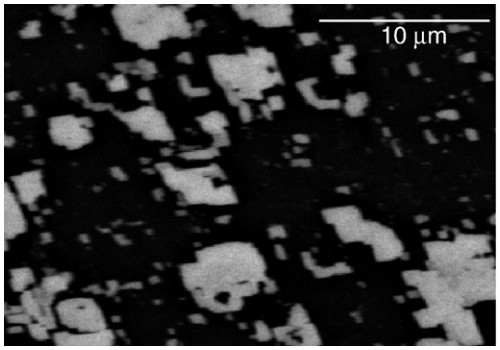

Fig. 11. Nucleation of $Cd_{0.97}Ca_{0.03}CO_3$ platelets (BSE-image) on the $\{10\bar{1}4\}$ surface of a calcite cleavage fragment.

candidate for removing cadmium from aqueous solutions. In spite of this, the removal of cadmium observed in sorption experiments performed in closed systems is disappointingly small. The uptake of cadmium by calcite becomes negligible when the concentration of cadmium in the fluid is still high (e.g. 0.078 mmol/l starting from a 0.1 mmol/l $CdCl_2$ solution), although the precipitate formed on calcite is very rich in cadmium ($X_{Cd}>0.97$). These uptake values contrast with the equilibrium end-points that can be calculated by solving the set of equilibrium, charge balance, and mass balance equations that describe the thermodynamics of this system. For example, starting with 100 cm^3 of a 0.1 mmol/l $CdCl_2$ aqueous solution and 2 g of calcite solids, equilibrium would require complete dissolution–recrystallization to form a unique and homogeneous Cd-poor solid phase ($X_{Cd}=4.98\cdot10^{-4}$) and an extremely Cd-poor aqueous solution ($7.00\cdot10^{-8}$ mmol/l).

As Prieto et al. (2003) have pointed out, an explanation of this apparent incongruity needs to consider the crystallographic relationships between the sorbate and the sorbent. In these experiments, the uptake of cadmium by calcite involves the release of solutes (Ca^{2+} and CO_3^{2-} ions) from the mineral surface to the fluid and the reaction between the dissolved solute and the aqueous Cd^{2+} ions to form the solid–solution overgrowth. Thus, calcite dissolution is concomitant with surface precipitation of $(Cd,Ca)CO_3$, resulting in a mechanism of sorption by dissolution–precipitation. However, in agreement with previous observations (Chiarello et al., 1997), the precipitate forms an epitaxial layer of nanometric thickness, which armours the substrate from further dissolution. As a consequence, the process stops when only a small amount of cadmium has been removed from the fluid. Obviously, at this stage, the system is not at equilibrium. However, the term "partial equilibrium" (Helgeson, 1968) could be used to describe a situation where the initial reacting solid becomes isolated from the aqueous solution by a coating of secondary solids that are at equilibrium with the fluid. Fig. 11 shows a backscattered electron image of the $(10\bar{1}4)$ surface of a typical calcite fragment where the incipient Cd-rich epitaxial overgrowth can be observed. The formation of such epitaxial layers can also be observed with AFM (Fig. 12).

The result is completely different when similar experiments are conducted using aragonite as a substrate. In such a case, the concentration of cadmium in the aqueous solution decays dramatically to reach values controlled by the extremely low solubility of the otavite end-member ($<2.2\cdot10^{-5}$ mmol/l in 30 days, starting from 0.1 mM $CdCl_2$). The process is also associated with simultaneous dissolution–precipitation, but in this case, substrate and overgrowth are not isostructural. The surface precipitate consists of rhombohedral calcite-type crystallites randomly oriented on the orthorhombic aragonite. Under these conditions, the amount of precipitate that can be formed without armouring the substrate surface from further dissolution is considerably larger than in the case of calcite. The concentration of dissolved cadmium decreases for months towards its virtually complete removal. During this process the aqueous phase becomes progressively Cd-poor and the precipitate eventually grows to become Ca-rich. As a consequence, the initial Cd-rich crystallites are ultimately surrounded by a calcium-rich rim and the main mass of pollutant becomes isolated from the fluid.

The previous examples illustrate that the reaction pathways in macroscopic sorption experiments can lead to partial equilibrium end-points (at least at a laboratory time-scale) that are not only determined by the thermodynamics of the SS–AS system but also by the crystallographic relationships between substrate and

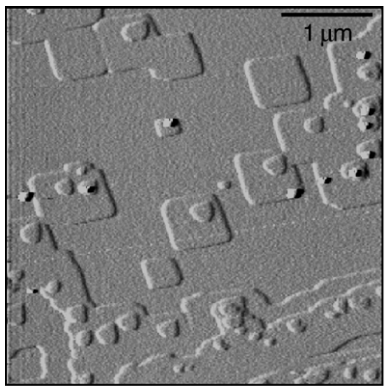

Fig. 12. AFM image showing $CdCO_3$ (otavite) two-dimensional nucleation on calcite $\{10\bar{1}4\}$ surface. Otavite nuclei show the typical rhombohedral morphology.

overgrowth. The formation of epitaxial layers results in an inhibiting effect that stops the sorption process when only a small amount of dissolved metal has been removed from the fluid. This effect is particularly evident when the structural matching between substrate and overgrowth is very good (Prieto et al., 2002).

7. The influence of newly formed nanolayers on subsequent growth: the template effect

It is well known that the presence of foreign ions can inhibit the normal growth of a pure crystal. Because the inhibition processes occur on mineral surfaces, AFM seems to be the most suitable technique to study such phenomena. AFM observations and measurements of the step velocity of monolayer growth advancement have provided information about the molecular mechanisms that control the inhibition of calcite growth in the presence of foreign ions. All the experiments carried out in the systems $(M,Ca)CO_3$–H_2O (M = Mn, Sr, and Mg) show that the growth rate of each monolayer strongly depends on the presence of the previous layer, and that the changes in the surface properties of the crystal can retard or even completely inhibit further growth, even when the aqueous solution is still supersaturated with respect to all possible solid solution compositions. Fig. 13 illustrates this phenomenon. The first image (a) was taken after flowing deionised water and immediately before the injection of a reacting solution. This led to the slight dissolution of calcite steps and the formation of etch pits with typical rhombohedral shape. The injection of a solution with very low concentration of Mn ($[MnCl_2]$ = 0.025 mmol/l) and supersaturated with respect to calcite ($\beta_{calcite}$ = 5.0) causes the lateral advancement of growth steps (a–c). However, a careful observation of the sequence indicates that only the first elementary growth layer (which is advancing on the original surface) grows perceptibly. This first newly formed substrate controls the subsequent surface evolution. At the beginning of the experiments, the advancement velocity of step 1 and step 2 is the same. However, whereas step 1 advances without restrictions, step 2 stops growing when it reaches the area formed by the step 1 advancement. This effect can be seen more clearly by observing the original etch pits. These etch pits are rapidly filled-in and the newly formed layer acts as a barrier preventing subsequent growth on it. Consequently, this area is surrounded by the next advancing step. This heterogeneous growth leads to an almost perfect reproduction of the topogra-

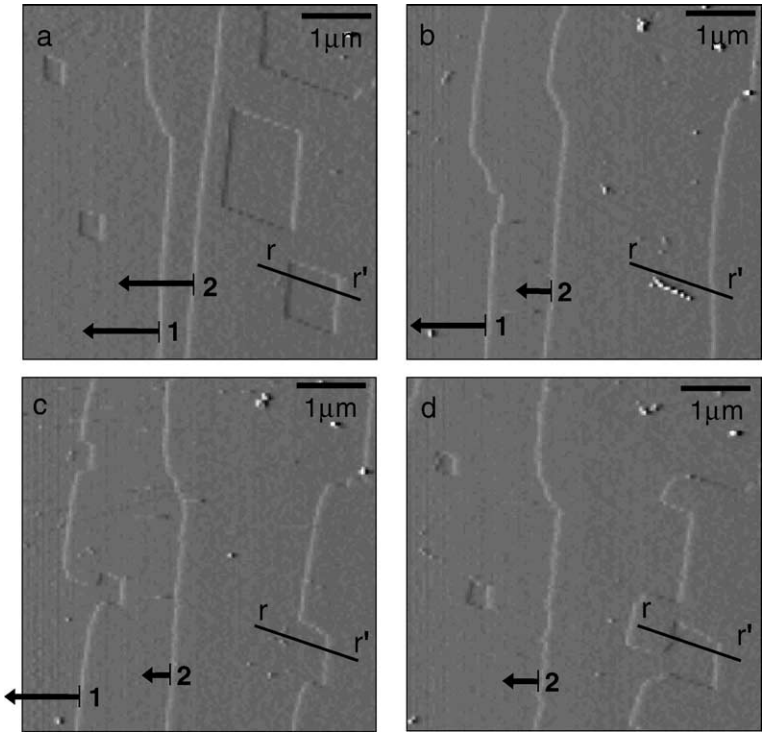

Fig. 13. (a–d) Growth sequence on a calcite $\{10\bar{1}4\}$ face in contact with a solution supersaturated with respect to calcite ($\beta_{calcite}$ = 5) and a small amount of Mn ($[MnCl_2]$ = 0.025mmol/l). The sequence shows the control of the surface on the growth process (template effect). The whole sequence of AFM images took 10 min approximately. A comparison of pictures (a) and (d) reveals the reproduction of the original microtopography.

phy of the original surface (compare Fig. 13a with d). We have called this phenomenon "template effect" because the original microtopography of the surface acts as a template that determines the subsequent evolution (Astilleros et al., 2002, 2003a,b; Freij et al., 2004). This effect has also been observed during growth of layers on dolomite cleavage surfaces from supersaturated solutions (Hu and Higgins, 2004).

A systematic analysis of the growth behaviour has shown a strong influence of both (a) the concentration of the foreign ion in the aqueous solution and (b) the thermodynamic properties of the overgrowing solid solution, on the effectiveness of the template effect. In general, the higher the impurity concentration in the aqueous solution, the stronger the reduction of step rates is and the clearer the reproduction of the original microtopography. Fig. 14 shows step advancement measurements from solutions with different amounts of Mn. On the other hand, whereas very small amounts of Mn in solution (Mn/Ca ≈ 0.1) cause a drastic reduction of the steps rates, considerable amounts of Mg and Sr (Sr/Ca and Mg/Ca > 1) are required to make the template effect appreciable. This different behaviour is related to the different tendency of these cations to incorporate in the calcite structure, which is very strong in the case of Mn (see Lorens, 1981; Mucci, 1988; Dromgoole and Walter, 1990; Pingitore et al., 1988) but weak for Sr and Mg (Böttcher, 1997; Mucci and Morse, 1983; Königsberger et al., 1999). Therefore, we can conclude that there is a direct relationship between the template effect and the amount of foreign ions incorporated in the newly formed layers. Although the ultimate reason for this behaviour is not well known, the fact that growth eventually stops at a

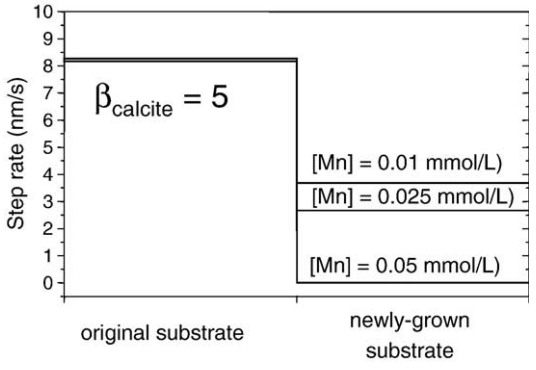

Fig. 14. Step advancement rates in contact with solutions supersaturated with respect to calcite ($\beta_{calcite}$) and different concentrations of Mn. The higher the Mn in solution the more effective is the effect of the newly formed substrate in inhibiting the subsequent step advancement, and the more exact is the reproduction of the pre-existing topography.

'buried' step edge suggests a difference between the lattice parameters of the new layers and the original steps. This can lead to the formation of a 'sub-nano step' at the original step edges.

The newly formed layers, with general composition $(M,Ca)CO_3$, limits coprecipitation as an effective mechanism for divalent metal uptake by hindering the normal crystal growth of solid solutions. It is important to note that this behaviour is not exclusive of calcite $\{10\bar{1}4\}$ surface, but it has also been observed on barite ($Ba(SO_4,CO_3)$–H_2O, $(Ba,Sr)SO_4$–H_2O) and celestite ($(Sr,Ba)SO_4$–H_2O) (001) surfaces (Astilleros et al., 2003b), which suggests that this is a general phenomenon in SS–AS systems.

8. Conclusions and future work

In the previous sections, we have illustrated the possibilities that AFM provides in the study of a number of phenomena that take place on calcite surfaces in presence of multicomponent aqueous solutions. Some of these phenomena can have important implications in crystal growth, which have not been taken into account so far. For example, the "template effect" seems to be a phenomenon that can affect both the growth behaviour and the composition of the growing phase. The differences in ionic radii of the substituting ions lead to the generation of a lattice mismatch between overgrowing and underlying layers, which in turn can cause a deviation from the equilibrium partitioning and the development of compositional zoning. Moreover, these observations have revealed a more active role of the surface in the growth process, whereas traditionally the emphasis has been placed on the aqueous solution composition and the degree of supersaturation.

The next step in the study of crystallization in SS–AS systems is to obtain further information of the relationships between the growing and underlying layer. This objective can only be reached if reliable data of the composition and structure of the forming layers is obtained. XPS and other suitable surface sensitive techniques can be used for this task. Lateral force microscopy (LFM), using frictional contrast between a substrate and a strained overlayer, could serve as a complementary technique to obtain a qualitative composition mapping, as Hay et al. (2003) have recently demonstrated. On the other hand, it will be necessary to check the universality of the "template effect" in the crystallization of solid solutions and to determine the thermodynamic, kinetic and crystallographic factors involved in its development. The metastable crystallization processes and the development of solvent-

mediated transformations are other aspects that deserve special attention in the case of crystallization of limited solid solutions.

Acknowledgements

J. M. Astilleros and Carlos M. Pina acknowledge financial support from Spanish Ministry of Science and Technology ("Ramon y Cajal" program). This work was partially supported by the Spanish Ministry of Science and Technology (Project BTE2002-00325) and the EU Network "Quantifying dissolution and precipitation of solid solutions in natural and industrial processes" (contract no. HPRN-CT-2000-058). **[LW]**

References

Astilleros, J.M, Pina, C.M., Fernández-Díaz, L., Putnis, A., 2000. Incorporation of barium on calcite ($10\bar{1}4$) surfaces during growth. Geochim. Cosmochim. Acta 64, 2965–2972.

Astilleros, J.M, Pina, C.M., Fernández-Díaz, L., Putnis, A., 2002. Molecular scale surface processes during the growth of calcite in the presence of manganese. Geochim. Cosmochim. Acta 66, 3177–3189.

Astilleros, J.M., Pina, C.M., Fernández-Díaz, L., Putnis, A., 2003a. Metastable phenomena on calcite $\{10\bar{1}4\}$ surfaces growing from Sr^{2+}–Ca^{2+}–CO_3^{2-} aqueous solutions. Chem. Geol. 193, 93–107.

Astilleros, J.M., Pina, C.M., Fernández-Díaz, L., Putnis, A., 2003b. Nanoscale growth of solids crystallising from multicomponent aqueous solutions. Surf. Sci. 545, L 767–L 773.

Astilleros, J.M., Pina, C.M., Fernández-Díaz, L., Putnis, A., 2003c. Supersaturation functions in binary solid solution–aqueous solution systems. Geochim. Cosmochim. Acta 67, 1601–1608.

Bokern, D.G., Ducker, W.A.C., Hunter, K.A., McGrath, K.M., 2002. Surface imaging of a natural mineral surface using scanning-probe microscopy. J. Cryst. Growth 246, 139–149.

Bosbach, D., Jordan, G., Rammensee, W., 1995. Crystal growth and dissolution kinetics of gypsum and fluorite: an in situ scanning force microscope study. Eur. J. Mineral. 7, 267–276.

Böttcher, M.E., 1997. Comment "Solid solution partitioning of Sr^{2+}, Ba^{2+}, and Cd^{2+} to calcite" by A.J. Tesoriero and J.F. Pankow. Geochim. Cosmochim. Acta 61, 661–662.

Cardew, P.T., Davey, R.J., 1985. The kinetics of solvent-mediated phase transformations. Proc. R. Soc. Lond., A 298, 415–428.

Chiarello, R.P., Sturchio, N.C., Grace, J.D., Geissbuhler, P., Sorensen, L.B., Cheng, L., Xu, S., 1997. Otavite–calcite solid–solution formation at the calcite–water interface studied in situ by synchrotron X-ray scattering. Geochim. Cosmochim. Acta 61, 1467–1474.

Davey, R., Garside, J., 2000. From molecules to crystallizers. An introduction to crystallization. Oxford Chemistry Primers vol. 86. Oxford University Press, Oxford. 81 pp.

Davis, J.A., Fuller, C.C., Cook, A.D., 1987. A model for trace metal sorption processes at the calcite surface: adsorption of Cd^{2+} and subsequent solid solution formation. Geochim. Cosmochim. Acta 51, 1477–1490.

De Giudici, G., 2002. Surface control vs. diffusion control during calcite dissolution: dependence of step-edge velocity upon solution pH. Am. Mineral. 87, 1279–1285.

Dromgoole, E.L., Walter, M., 1990. Inhibition of calcite growth rates by Mn^{2+} in $CaCl_2$ solutions at 10, 25 and 50 °C. Geochim. Cosmochim. Acta 54, 2991–3000.

Freij, S.J., Putnis, A., Astilleros, J.M., 2004. Nanoscale observations of the effect of cobalt on calcite growth and dissolution. J. Cryst. Growth 267, 288–300.

Glynn, P.D., 2000. Solid–solution solubilities and thermodynamics: sulfates, carbonates and halides. Sulfate Minerals: Crystallography, Geochemistry and Environmental Significance, Reviews in Mineralogy and Geochemistry, vol. 40, pp. 481–511.

Glynn, P.D., Reardon, E.J., 1990. Solid-solution aqueous-solution equilibria: thermodynamic theory and representation. Am. J. Sci. 290, 164–201.

Godelitsas, A., Astilleros, J.M., Hallam, K., Harissopoulos, S., Putnis, A., 2003. Interaction of calcium carbonates with lead in aqueous solutions. Environ. Sci. Technol. 37, 3351–3360.

Hartman, P., Perdok, W.G., 1955. On the relations between structure and morphology of crystals. I. Acta Crystallogr. 8, 49–52.

Hay, M.B., Workman, R.K., Manne, S., 2003. Mechanisms of metal ion sorption on calcite: composition mapping by lateral force microscopy. Langmuir 19, 3727–3740.

Heijnen, W.M.M., 1985. The morphology of gel grown calcite. N. Jb. Mineral. Mh. 8, 357–371.

Helgeson, H.C., 1968. Evaluation of irreversible reactions in geochemical processes involving minerals and aqueous solutions: I. Thermodynamic relations. Geochim. Cosmochim. Acta 32, 853–877.

Hillner, P.E., Gratz, A.J., Manne, S., Hansma, P.K., 1992. Atomic-scale imaging of calcite growth and dissolution in real time. Geology 20, 359–362.

Hu, X., Higgins, S.R., 2004. Dolomite surface kinetics and composition from supersaturated and undersaturated non-stoichiometric solutions. Geochim. Cosmochim. Acta 68, A134.

Jordan, G., Rammensee, W., 1998. Dissolution rates of calcite ($10\bar{1}4$) surfaces obtained by scanning force microscopy: microtopography-based dissolution kinetics on surfaces with anisotropic velocities. Geochim. Cosmochim. Acta 62, 941–947.

Jordan, G., Higgins, S.R., Eggleston, C.M., Knauss, K.G., Schmahl, W.W., 2001. Dissolution kinetics of magnesite in acidic aqueous solution, a hydrothermal atomic force microscopy (HAFM) study: step orientation and kink dynamics. Geochim. Cosmochim. Acta 65, 4257–4266.

Kelly, S.D., Newville, M.G., Cheng, L., Kemmer, K.M., Sutton, S.R., Fenter, P., Sturchio, N.C., Spölt, C., 2003. Uranyl incorporation in natural calcite. Environ. Sci. Technol. 37, 1284–1287.

Königsberger, E., Königsberger, L.C., Gamsjäger, H., 1999. Low-temperature thermodynamic model for the system Na_2CO_3–$MgCO_3$–$CaCO_3$–H_2O. Geochim. Cosmochim. Acta 63, 3105–3119.

Liang, Y., Baer, D.R., McCoy, J.M., LaFemina, J.P., 1996. Interplay between step velocity and morphology during the dissolution of $CaCO_3$ surface. J. Vac. Sci. Technol., A, Vac. Surf. Films 14 (3), 1368–1375.

Lippmann, F., 1980. diagrams depicting the aqueous solubility of mineral systems. N. Jb. Mineral. Abh. 139 (1), 1–25.

Lorens, R.B., 1981. Sr, Cd, Mn and Co distribution coefficients in calcite as a function of calcite precipitation rate. Geochim. Cosmochim. Acta 45, 553–561.

McBeath, M.K., Rock, P.A., Casey, W.H., Mandell, G.K., 1998. Gibbs energies of formation of metal-carbonate solid solutions: Part 3. The $Ca_xMn_{1-x}CO_3$ system at 298 K and 1 bar. Geochim. Cosmochim. Acta 62, 2799–2808.

Mucci, A., 1988. Manganese uptake during calcite precipitation from seawater: conditions leading to the formation of pseudokutnahorite. Geochim. Cosmochim. Acta 52, 1859–1868.

Mucci, A., Morse, J.W., 1983. The incorporation of Mg^{2+} and Sr^{2+} into calcite overgrowths. Geochim. Cosmochim. Acta 47, 217–233.

Mucci, A., Morse, J.W., 1990. Chemistry of low-temperature abiotic calcites: experimental studies on coprecipitation, stability and fractionation. Aquat. Sci. 3, 217–254.

Paquette, J., Reeder, R.J., 1990. New type of compositional zoning in calcite: insights into crystal growth mechanisms. Geology 18, 1244–1247.

Paquette, J., Reeder, R.J., 1995. Relationship between surface structure, growth mechanism, and trace element incorporation in calcite. Geochim. Cosmochim. Acta 59, 735–749.

Pina, C.M., Becker, U., Risthaus, P., Bosbach, D., Putnis, A., 1998a. Molecular-scale mechanisms of crystal growth in barite. Nature 395, 483–486.

Pina, C.M., Bosbach, D., Prieto, M., Putnis, A., 1998b. Microtopography of the barite (001) face during growth: AFM observations and PBC theory. J. Cryst. Growth 187, 119–125.

Pina, C.M., Enders, M., Putnis, A., 2000a. The composition of solid solutions crystallising from aqueous solutions: the influence of supersaturation and growth mechanisms. Chem. Geol. 168, 195–210.

Pina, C.M., Fernández-Díaz, L., Prieto, M., Putnis, A., 2000b. In situ atomic force microscope observations of a dissolution–crystallisation reaction: the phoshenite–cerussite transformation. Geochim. Cosmochim. Acta 64, 215–221.

Pina, C.M., Putnis, A., y Astilleros, J.M., 2004. The growth mechanisms of solid solutions crystallising from aqueous solutions. Chem. Geol. 204, 145–161.

Pingitore Jr., N.E., 1986. Modes of coprecipitation of Ba^{2+} and Sr^{2+} with calcite. In: Davis, J.A., Hayes, K.F. (Eds.), Geochemical Processes at Mineral Surfaces, ACS Symp. Ser. vol. 323. , pp. 574–586.

Pingitore Jr., N.E., Eastman, M.P., Sandige, M., Oden, K., Freiha, B., 1988. The coprecipitation of manganese(II) with calcite: an experimental study. Mar. Chem. 25, 107–120.

Piriou, B., Fedoroff, M., Jeanjean, J., Bercis, L., 1997. Characterization of sorption of europium(III) on calcite by site-selective and time-resolved luminescence spectroscopy. J. Colloid Interface Sci. 194, 440–447.

Plummer, L.N, Busenberg, E., 1982. The solubilities of calcite, aragonite and vaterite in CO_2–H_2O solutions between 0 and 90 °C, and an evaluation of the aqueous model for the system $CaCO_3$–CO_2–H_2O. Geochim. Cosmochim. Acta 46, 1011–1040.

Plummer, L.N., Busenberg, E., 1987. Thermodynamics of aragonite–strontianite solid solutions: results from stoichiometric solubility at 25 and 76 °C. Geochim. Cosmochim. Acta 51, 1393–1411.

Prieto, M., Putnis, A., Fernández-Díaz, L., 1993. Crystallization of solid solutions from aqueous solutions in a porous medium: zoning in (Ba,Sr)SO_4. Geol. Mag. 130, 289–299.

Prieto, M., Fernández-González, A., Putnis, A., Fernández-Díaz, L., 1997. Nucleation, growth and zoning phenomena in crystallizing (Ba,Sr)CO_3, Ba(SO_4,CrO_4), (Ba,Sr)SO_4, and (Cd,Ca)CO_3 solid solutions from aqueous solutions. Geochim. Cosmochim. Acta 61, 3383–3397.

Prieto, M., Fernández-González, A., Martín-Díaz, R., 2002. Sorption of chromate ions diffusing through barite–hydrogel composites: implications for the fate and transport of chromium in the environment. Geochim. Cosmochim. Acta 66, 783–795.

Prieto, M., Cubillas, P., Fernández-González, A., 2003. Uptake of dissolved Cd by biogenic and biogenic aragonite: a comparison with sorption onto calcite. Geochim. Cosmochim. Acta 67, 3859–3869.

Reeder, R.J., 1996. Interaction of divalent cobalt, zinc, cadmium, and barium with the calcite surface during layer growth. Geochim. Cosmochim. Acta 60, 1543–1552.

Reeder, R., Lamble, G.M., Northrup, P.A., 1999. XAFS study of the coordination and local relaxation around Co^{2+}, Zn^{2+}, Pb^{2+}, and Ba^{2+} trace elements in calcite. Am. Mineral. 84, 1049–1060.

Reeder, R., Nugent, M., Lamble, G.M., Tait, C.D., Morris, D.E., 2000. Uranyl incorporation into calcite and aragonite: XAFS and luminiscence studies. Environ. Sci. Technol. 34, 638–644.

Rimstidt, J.D., Balog, A., Webb, J., 1998. Distribution of trace elements between carbonate minerals aqueous solutions. Geochim. Cosmochim. Acta 62, 1851–1863.

Shiraki, R., Rock, P.A., Casey, W.H., 2000. Dissolution kinetics of calcite in 0.1 M NaCl solution at room temperature: an atomic force microscopic (AFM) study. Aquat. Geochem. 5, 87–108.

Staudt, W.J., Reeder, R.J., Schoonen, M.A.A., 1994. Surface structural controls on compositional zoning of SO_4^{2-} and SeO_4^{2-} in synthetic calcite crystals. Geochim. Cosmochim. Acta 58, 2087–2098.

Stipp, S.L., Hochella, M.F., Parks, G.A., Leckie, J.O., 1992. Cd^{2+} uptake by calcite, solid-state diffusion, and the formation of solid-solution: interface processes observed with near-surface sensitive techniques (XPS, LEED, and AES). Geochim. Cosmochim. Acta 56, 1941–1954.

Stipp, S.L., Parks, G.A., Nordstrom, D.K., Leckie, J.O., 1993. Solubility-product constant and thermodynamic properties for synthetic otavite, $CdCO_3$(s), and aqueous association constants for the Cd(II)–CO_2–H_2O system. Geochim. Cosmochim. Acta 57, 2699–2713.

Stipp, S.L.S., Lakshtanov, L.Z., Jensen, J.T., Baker, J.A., 2003. Eu^{3+} uptake by calcite: preliminary results from coprecipitation experiments and observations with surface-sensitive techniques. J. Contam. Hydrol. 61, 33–43.

Sturchio, N.C., Antonio, M.R., Soderholm, L., Sutton, S.R., Brannon, J.C., 1998. Tetravalent uranium in calcite. Science 281, 971–973.

Sturchio, N.C., Chiarello, R.P., Cheng, L., Lyman, P.F., Bedzyk, M.J., Qian, Y., You, H., Yee, D., Geissbuhler, P., Sorensen, L.B., Liang, Y., Baer, D.R., 1997. Lead adsorption at the calcite–water interface: synchroton X-ray standing wave and X-ray reflectivity studies. Geochim. Cosmochim. Acta 61, 251–263.

Sunagawa, I., 1987. Morphology of minerals. In: Sunagawa, I. (Ed.), Morphology of Crystals. TERRAPUB, Tokyo.

Tesoriero, A.J., Pankow, J.F., 1996. Solid solution partitioning of Sr^{2+}, Ba^{2+}, and Cd^{2+} to calcite. Geochim. Cosmochim. Acta 60, 1053–1063.

Zachara, J.M., Cowan, C.E., Resch, C.T., 1991. Sorption of divalent metals on calcite. Geochim. Cosmochim. Acta 55, 1549–1562.